

# **Simulating the Measurement of the Electron Beam Emittance at AWAKE**

Patrick Chin

March 27, 2017

Department of Physics & Astronomy,  
University College London

Supervised by Prof. M. Wing  
& Dr. S. Jolly

## Abstract

In preparation for experiments at AWAKE in CERN, simulations of the beam and measuring of the beam's parameters were carried out. This was done in order to investigate how the measurement of the emittance of the beam behaves under changes to experimental parameters. The energy spread of the beam was investigated and a minimum percentage energy spread of 4 % was found to be the cutoff point at which measurements become reliable. Emittance values were investigated and emittances above  $10^{-5}$  mrad were found to be measured inaccurately. Background photon values up to  $10^4$  times the expected background were simulated, showing accurate measurements up to a factor of  $\sim 4 \times 10^2$ , above which the measured emittance deviated significantly from the true value. Improvements and limitations of the simulation due to assumptions made are also discussed.

# Contents

<b>1</b>	<b>Introduction</b>	<b>4</b>
<b>2</b>	<b>Plasma Wakefield Acceleration</b>	<b>4</b>
2.1	The AWAKE Project . . . . .	5
2.1.1	Proton Bunch Length . . . . .	5
2.1.2	Uniform Density Plasma Cell . . . . .	5
2.1.3	Injection of the Witness Beam . . . . .	6
2.1.4	AWAKE Overview . . . . .	6
<b>3</b>	<b>Spectrometer</b>	<b>6</b>
3.1	Design Overview . . . . .	7
<b>4</b>	<b>Theory</b>	<b>7</b>
4.1	Single Particle Dynamics . . . . .	7
4.2	Emittance . . . . .	7
<b>5</b>	<b>The Simulation</b>	<b>8</b>
5.1	The Electron Beam . . . . .	8
5.1.1	BDSIM Calibration . . . . .	9
5.1.2	Deriving the Beam Size Function . . . . .	9
5.2	Backgrounds . . . . .	10
5.2.1	Error Calculations . . . . .	11
5.3	Calculating the Emittance . . . . .	12
<b>6</b>	<b>Results</b>	<b>12</b>
6.1	Binning errors . . . . .	12
6.2	Energy Spread . . . . .	12
6.3	Input Emittance . . . . .	15
6.4	Background Photons . . . . .	15
<b>7</b>	<b>Conclusion</b>	<b>15</b>

# 1 Introduction

Advancements in quantum and particle physics are primarily driven by experimental observations, which can verify or refute previous hypotheses, or can provide data from which new hypotheses can be drawn. The overall goal is to gain a deeper understanding of the universe around us. Particle colliders are a main source of observational data at the quantum scale, and can create millions of collision events every second. Design modifications to these colliders mostly increase the luminosity of the colliding beams in order to produce more data. This report however, focuses on a design modification aimed at increasing the energy of the colliding beams. This will allow the investigation of energy regions that have yet to be reached, thus allowing the observation of particle interactions that only happen at higher energies. These interactions may give insight into questions pertaining to the unification of the fundamental forces.

Beams at the Large Hadron Collider (LHC) operated at centre-of-mass energies of 7 TeV and 8 TeV [1] in the quest to find the Higgs Boson, and proton–proton centre-of-mass energies at CERN have recently reached 13 TeV [2]. Lepton–lepton colliders, however, have yet to reach the TeV energy milestone. The largest lepton–lepton collider, the Large Electron-Proton Collider (LEP), was closed down to make way for the LHC in 2000 after having reached a maximum energy of 209 GeV [3].

The appeal of colliding leptons over composite particles such as protons arises from the fact that leptons are fundamental point-like particles. Their centre-of-mass energy can be more accurately determined and collisions between leptons produce a much cleaner environment, allowing for easier observation of the resultant particles and simpler analysis of the data.

Circular accelerators, such as LEP, have a major drawback when accelerating leptons, and that is the loss of a particle’s energy due to synchrotron radiation, which limits the focusing of electron beams [4]. This is the emittance of radiation from relativistic charged particles that are moving in a uniform magnetic field. The energy loss is inversely proportional to the fourth power of the rest mass of the particle [5], meaning that electrons lose more energy than protons by a factor of about  $10^{13}$  which is one of the main reasons why protons are being collided at

CERN rather than electrons. During experiments performed at the LEP the radiated power when running at 100 GeV reached about 18 MW which needs to be resupplied to the beam just to keep it’s circular trajectory.

This problem can be overcome by creating linear particle accelerators. There are currently two radio-frequency (RF) linear lepton–lepton accelerator proposals, the Compact Linear Collider (CLIC) [6] and the International Linear Collider (ILC) [7] which are expected to reach collision energies of up to several TeV and 500 GeV respectively. With current RF technology, the continuous scaling of linear lepton–lepton accelerators to higher and higher energies, requires greater accelerator lengths extending to the 100 km scale for collisions in the TeV scale. Building accelerators of this scale is deemed impractical for most situations due to geographical and financial limitations. This urges the development of new technologies in order to continue pushing the energy frontier of particle accelerators while scaling down their lengths.

## 2 Plasma Wakefield Acceleration

Current RF accelerator technology is limited to an electromagnetic gradient of about  $100 \text{ MV m}^{-1}$  due to material breakdown in the walls of the structure. The ability of plasma to sustain very large electromagnetic fields makes it a good candidate for a medium within which charged particles can be accelerated. The concept being that the plasma can act as an energy transfer medium, removing energy from a driver beam, such as a laser or a proton beam, and transferring it to a bunch of charged leptons. As the driver beam travels through the plasma cell, it leaves an oscillating electromagnetic field in it’s wake. The beam to be accelerated (the witness beam) is injected ahead of a propagating electromagnetic wave as shown in Figure 1b where it is accelerated under the electromagnetic gradient. In 1979, the concept of laser plasma acceleration was shown in simulations to be of practical use in accelerators and pulsers [8]. More recently, proof-of-concept experiments implementing laser plasma acceleration have been shown to accelerate electrons to the GeV scale in a cm-scale plasma cell [9, 10], providing results that are consistent with simulations.

## 2.1 The AWAKE Project

Simulations of plasma wakefield accelerators driven by proton beams were carried out in 2009 [11], showing the high energy transfer efficiency between a driver proton bunch and an electron witness bunch. In these simulations, a 1 TeV proton beam drove the wakefield in a 400 m long plasma cell, which accelerated a 10 GeV electron beam to 650 GeV, displaying gradients of over  $1 \text{ GV m}^{-1}$  which is about ten times larger than current accelerators. The AWAKE project is a proof-of-concept experiment for proton driven plasma wakefield acceleration with the goal of accelerating 15 MeV electrons up to  $\sim 1.3 \text{ GeV}$  over a distance of 10 m. Later, aiming to reach 10 GeV in the same distance, demonstrating electromagnetic gradients in the  $\text{GV m}^{-1}$  scale as displayed in the simulation.

A few challenges arose during the design of this experiment.

### 2.1.1 Proton Bunch Length

The first challenge in the development of this accelerator was getting the length of the proton driver bunch small enough such that it is able to create resonant waves in the plasma, where the plasma wavelength  $\lambda_{pe} \approx 1.26 \text{ mm}$ . Typical proton bunches, such as those produced by the CERN Super Proton Synchrotron (SPS), have lengths of  $\sim 10 \text{ cm}$  which alone, cannot create strong plasma waves at the required wavelength, as the Fourier component of the proton beam at the plasma frequency is negligible.

Simulations on the compression of these proton bunches to such small lengths [12], show that reducing the longitudinal phase volume blows up the transverse phase volume, resulting in a diverging beam with a large emittance. An alternative method would be to split up the proton bunch into a number of micro-bunches to be simultaneously decelerated, all of which contribute energy to the wakefield. This means that a 10 cm proton bunch will need to be split into  $\sim 100$  micro-bunches in order to be able to drive the wake.

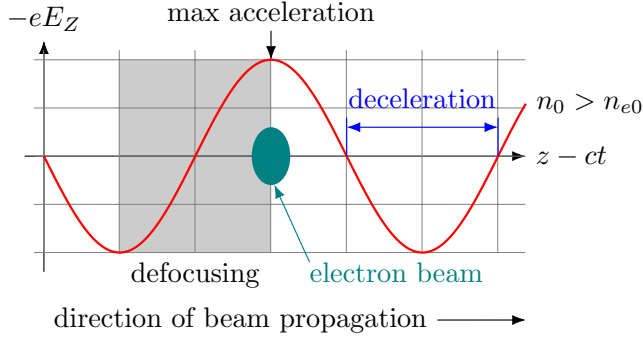
The splitting of the proton beam can be achieved by using an instability between the beam and the plasma which arises from the mutual amplification of the rippling of the beam radius and the plasma wave, known as self-modulated instability (SMI). This instability tends to destroy the plasma wave

as the amplification focuses and defocuses various parts of the beam. However, by seeding the SMI with a short electron bunch [13], a laser pulse [14] or a sharp cut in the bunch profile [12], a single mode of the oscillating plasma wave and beam rippling will be promoted while other modes, including the strongest competing modes, the hosing modes [15] will be suppressed. This produces well-separated micro-bunches of protons with of a short enough length to induce a plasma wave at the resonance frequency of the plasma.

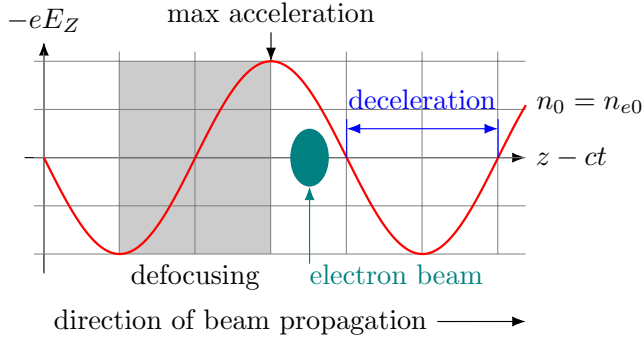
### 2.1.2 Uniform Density Plasma Cell

All proton micro-bunches contribute to the wakefield, and only if the plasma density is uniform, will the contribution of each bunch be coherent. Incoherent proton bunches will cause alterations in the plasma wakefield meaning that the electron bunches will arrive at the wrong phase of the plasma wave's oscillation. An increase in the plasma density will shorten the plasma wavelength, causing it to gain on the electron bunch allowing electrons to crest plasma wave it was riding and fall into the defocusing phase of the plasma wave as shown in Figure 1a. A decrease in the plasma density will increase the plasma wavelength causing the plasma wave to fall further behind the electron bunch meaning the electron bunch to fall into the trough of the plasma wave, resulting in a deceleration of the electron beam as shown in Figure 1c. The electron beam must be in the region, of length  $\lambda_{pe}/4$ , between the defocusing and decelerating phases of the plasma wave in order to be appropriately accelerated. These effects also affect the proton beam, however due to their large longitudinal momentum, are influenced to a much lesser degree.

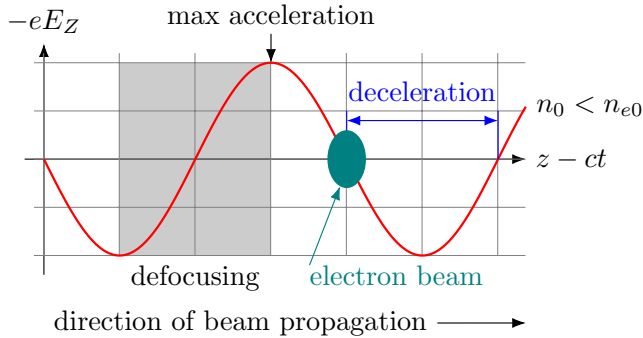
This requirement of the plasma, limits the plasma selection to being uniform rubidium vapor, ionised by a co-propagating laser pulse [17, 18]. Rubidium was chosen due to it's low ionization potential and heavy atomic mass. A heavy element is required to minimize the movement of the plasma's nuclei, which causes adverse effects to the plasma's behaviour [19, 20]. The Rubidium vapor is kept in thermodynamic equilibrium at a constant temperature and volume in order to keep it's density as uniform as possible.



(a) Injection of the electrons for a shorter plasma wavelength, where electrons may crest the wave.



(b) Injecting at the ideal phase, where all electrons will be accelerated.



(c) Injection for a longer plasma wavelength, where electrons may fall into the deceleration region.

Figure 1: Phase of the injection of the electron beam [16].

### 2.1.3 Injection of the Witness Beam

Due to SMI, the shape of the drive beam changes in the plasma and for the first four meters, the difference between the phase velocity of the wakefield and the proton beam velocity is quite large and this will effect the electron beam in the same manner as having a non uniform plasma. To avoid this problem it was suggested that the electrons be injected into the plasma after SMI had fully developed at  $\sim 4\text{m}$  into the plasma. The design of the injection method eventually arrived at passing the electron beam through a narrow vacuum tube separated from

the plasma by a thin foil, then after the required distance the electrons will be directed into the wakefield close behind the many proton bunches driving the wakefield.

### 2.1.4 AWAKE Overview

The SPS will provide a 400 GeV proton beam with a bunch length of  $\sigma_z = 12\text{cm}$  and an intensity of  $\sim 3 \times 10^{11}$  protons per bunch. This will travel down the 750 m long proton beam line, previously used for the CERN Neutrinos to Gran Sasso project (CNGS), and will be focused in-front of the plasma cell to a horizontal and vertical beam size of  $\sigma_{x,y} = 200\text{ }\mu\text{m}$ . It will then enter the 10 m long Rubidium vapor plasma cell with an adjustable density at the  $10^{14}$  to  $10^{15}$  electrons/cm scale. The proton driver will self modulate at the plasma wavelength  $\lambda_{pe}$  after being seeded by a high powered  $\sim 4.5\text{ TW}$  laser pulse that is co-axial and co-propagating with the proton driver beam. This laser also serves the purpose of ionising the Rubidium vapor to create the plasma. For these beams to be co-axial for the full length of the plasma cell, they need to be synchronous to within 100 ps and the size of the focal point of the proton beam is required to be  $\leq 100\text{ }\mu\text{m}$  and  $\leq 15\text{ }\mu\text{rad}$

The electron witness beam will be created via photo-emission by an illuminating cathode electron source. It will then be accelerated by a 2.5 cell RF-gun and a meter long booster at both at 3 GHz. This will accelerate the beam up to 20 MeV and an energy spread of 0.5 %, before it is injected into the plasma cell to be further accelerated to  $\sim 1.3\text{ GeV}$ . The accelerated beam will then exit the 10 m long plasma cell to be analysed by the spectrometer.

## 3 Spectrometer

There are two main goals the spectrometer is expected to fulfill. The first is to measure the mean energy and energy spread of the beam, as it is this measurement that determines the success of the AWAKE project, i.e. whether or not the electrons were accelerated up to the desired 1.3 GeV, which would demonstrate the use of large EM gradients of  $\sim 1\text{ GV m}^{-1}$ . The second goal it to measure the quality of the beam which can quantitatively be de-

scribed by its emittance which is defined in Section 4.2.

### 3.1 Design Overview

A C-shaped dipole magnet with a maximum setting of 650 A is placed downstream of the plasma cell in order to separate the electron and proton beams, as well as measure the energy and energy spread of the beam by deflecting electrons onto a 65 mm high by 1 m wide scintillator screen. The amount by which each electron is deflected, and hence its horizontal position on the screen, can be directly related to its energy. To improve the ratio of the electron beam signal to the background noise, a quadrupole doublet is placed upstream of the dipole. This will focus electrons that are at a certain energy onto the screen and under or over-focus electrons that are at different energies. This will result in a vertical spread of electrons that are tightly focused at the horizontal position on the screen pertaining to the mean energy of the beam, gradually becoming less focused and more spread out further from this horizontal position. The emittance of the beam cannot directly be measured since it is a measure of both the beam size and beam divergence. However from the shape of the incident beam on the screen and an understanding of the effects of the quadrupole and the dipole, a function can be derived which calculates the initial emittance of the beam.

Due to large amounts of background radiation in the main tunnel, the intensified CCD camera (Andor iStar 340T) will be situated 17 m from the screen in an adjacent tunnel. Light from the screen will be reflected onto the camera using a series of mirrors [21] and the goals of the spectrometer will be achieved by analysing the signal received by this camera.

## 4 Theory

### 4.1 Single Particle Dynamics

When working with beams of particles, it is advantageous to work in the coordinate system that follows the ideal path of the beam, denoting this axis with  $z$ . A particle's state can be described with the coordinates  $(u, u')$  that lie in what is known as phase space, where  $u$  is a plane transverse to the direction of the propagating beam, either  $x$  or  $y$ , and  $u'$  is

the transverse velocity of the particle in the  $u$  plane. If the beam's motion in these transverse planes are independent, that is, we ignore transverse coupling terms, a particle's motion in each plane can be described by

$$\begin{pmatrix} u(z) \\ u'(z) \end{pmatrix} = \begin{pmatrix} C_u(z) & S_u(z) \\ C'_u(z) & S'_u(z) \end{pmatrix} \begin{pmatrix} u_0 \\ u'_0 \end{pmatrix} \quad (1)$$

where the functions  $C_u(z)$ ,  $S_u(z)$ ,  $C'_u(z)$  and  $S'_u(z)$ , describe the effect the beam line has on the position and divergence of an individual particle. Using this system of matrices, drift and quadrupole matrices can be derived [16] where the drift matrix is

$$\mathcal{M}_D(l) = \begin{pmatrix} 1 & l \\ 0 & 1 \end{pmatrix} \quad (2)$$

the matrix of a focusing quadrupole of length  $l$  and strength  $k$  is

$$\mathcal{M}_{QF}(l) = \begin{pmatrix} \cos \varphi & \frac{1}{\sqrt{k}} \sin \varphi \\ -\sqrt{k} \sin \varphi & \cos \varphi \end{pmatrix} \quad (3)$$

where  $\varphi = \sqrt{k}l$ . The matrix of a defocusing quadrupole is

$$\mathcal{M}_{QD}(l) = \begin{pmatrix} \cosh \varphi & \frac{1}{\sqrt{|k|}} \sinh \varphi \\ -\sqrt{|k|} \sinh \varphi & \cosh \varphi \end{pmatrix} \quad (4)$$

where  $\varphi = \sqrt{|k|}l$ .

These transport matrices can be multiplied together resulting in the transformation matrix representing all the components of a beamline, making it simple to follow a particle down a transport line.

### 4.2 Emittance

Grouping the individual particles of a beam, they will occupy an area in phase space known as the emittance. Qualitatively the emittance of a beam is a measure of how parallel the particles of the beam are to each other and is a conserved quantity while the beam is not being acted upon by external forces.

In phase space the beam of particles will usually take up an area resembling that of an ellipse. This is because, after a diverging or converging beam has traveled through an aperture, we expect particles that are further away from the centre of the beam to have a larger transverse momentum. This is unless the beam is being measured at its waist where



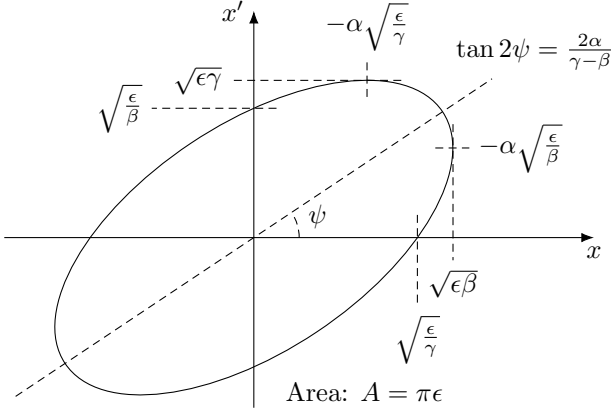


Figure 2: A representation of the relation between the Twiss parameters of a beam's ellipse in phase space [16].

it is transitioning between converging and diverging or visa versa. Figure 2 shows the projection of a beam, diverging in the  $x$  direction, onto the two dimensional  $x$  phase space. A line in the shape of an ellipse is drawn such that it encompasses 95 % of all the particles in the beam [22], this is called the phase ellipse. The emittance is defined by the area of this ellipse divided by  $\pi$  in units of mrad. Note that in general, the transverse momenta, hence the slope of the particles in the beam, are very small so the approximation  $\sin u' \approx u'$  can be used.

The general equation of an ellipse can be used to describe the phase ellipse:

$$\gamma x^2 + 2\alpha x x' + \beta x'^2 = \epsilon \quad (5)$$

where  $\alpha$ ,  $\beta$ ,  $\gamma$  and  $\epsilon$  are ellipse parameters that determine the ellipse's shape and orientation in phase space. The area of the ellipse  $\epsilon$  is defined as the emittance<sup>1</sup>. Of the four beam parameters, only three are independent, and since  $\epsilon$  is defined as the area, the other three can be found to be correlated from the ellipse's geometric properties by

$$\beta\gamma - \alpha^2 = 1 \quad (6)$$

A matrix describing the beam, the beam matrix, has been derived using the matrix representation of the ellipse. The beam matrix allows the whole beam to be transported via the transport matrices in (2), (4) and (3) [16]. This beam matrix is defined as

$$\sigma = \begin{pmatrix} \sigma_{11} & \sigma_{12} \\ \sigma_{21} & \sigma_{22} \end{pmatrix} = \epsilon \begin{pmatrix} \beta & -\alpha \\ -\alpha & \gamma \end{pmatrix} \quad (7)$$

<sup>1</sup>Often, the units of  $\pi$  are omitted and the emittance is given in units of  $\pi$  mrad.

where each element describes distributions of particles in the beam as follows:

$$\sigma_{11} = \langle x_i^2 \rangle = \epsilon\beta \quad (8)$$

$$\sigma_{22} = \langle x_i'^2 \rangle = \epsilon\gamma \quad (9)$$

$$\sigma_{12} = \langle x_i x_i' \rangle = -\epsilon\alpha \quad (10)$$

The evolution of this matrix along the beam transport line can then be calculated by applying the transport matrix to the beam matrix:

$$\sigma_1 = \mathcal{M} \sigma_0 \mathcal{M}^T \quad (11)$$

where  $\sigma_0$  is the initial beam matrix,  $\mathcal{M}$  is the transport matrix of the beam line and  $\sigma_1$  is the beam matrix at the end of the beam line.

## 5 The Simulation

The simulation of this experiment was split into three parts: the simulation of the beam, the simulation of the effects of the background and camera, and the reconstruction of the beam in order to measure the parameters of the beam.

### 5.1 The Electron Beam

Given enough computing power and time, the simulation of the beam, from the end of the plasma cell, passing through two quadrupoles and through a dipole and hitting the scintillator screen could have been done on BDSIM [23], a Geant4 [24] toolkit for simulating radiation traveling through an accelerator and accelerator components. This software package simulates the motion of each particle individually, updating it's position and velocity at each step through the accelerator by applying forces from the fields of each component of the accelerator. For beams consisting of  $\sim 10^9$  particles, tracking each particle individually as they travel down the beam line would take enormous amounts of time and available computing power, and, as this simulation was required to be performed a large number of times, this would have been impractical for obtaining any reasonable amount of data.

A new program was written, taking advantage of beam matrices to describe the beam as a whole. The goal of the first part of this program is to simulate the intensity of the incident beam at each pixel on the screen.



Parameter	Value
Screen and Camera	
Screen width	1 m
Screen height	65 mm
Horizontal pixels	1850
Screen efficiency	5000 photons/electron
Camera acceptance	$1.5 \times 10^{-5}$
Camera MCP Gain	1442
Camera quantum efficiency	0.15
Accelerated electron beam	
Emittance ( $\epsilon$ )	$1 \times 10^{-6}$ m rad
Mean energy ( $\bar{E}$ )	1.3 GeV
Energy spread ( $\sigma_E$ )	0.4 GeV
Electrons/bunch ( $N_{e^-}$ )	$1 \times 10^9$
Background photon density	$3.415 \times 10^4$ m $^{-2}$

Table 1: The expected values for many experimental parameters have been calculated.

### 5.1.1 BDSIM Calibration

The effect of the quadrupole and the dipole are dependant on the energy of the individual electrons in the beam. So to calculate the density and energy of the electrons as a function of the horizontal screen position a number of BDSIM simulations were run.  $1 \times 10^5$  electrons were fired individually down the simulated AWAKE beam line. These electrons had a square energy distribution from 0 TeV to 10 TeV, and had a Gaussian spacial distribution with  $\sigma_x = \sigma_y = 6$  mm (this is the size of the iris at the end of the plasma), and no transverse momentum. This large energy range was chosen to encompass the entire energy range that would hit the screen. The dipole was set to it's highest setting of 650 A to achieve the maximum spread of the beam on the screen.

These BDSIM runs were used to plot the function in Figure 3a which shows the relationship between an electron's energy and where it is expected to hit the screen. Figure 3b is an example of the horizontal distribution of a beam of electrons, with a Gaussian energy spread, onto the screen and all other experimental parameters set to their expected default value. This was calculated by applying  $x(E)$ , the inverse of the function  $E(x)$  shown in Figure 3a, to the energy distribution of the beam.

At these settings of the experiment, all of the electrons of the beam hit the screen, allowing for an

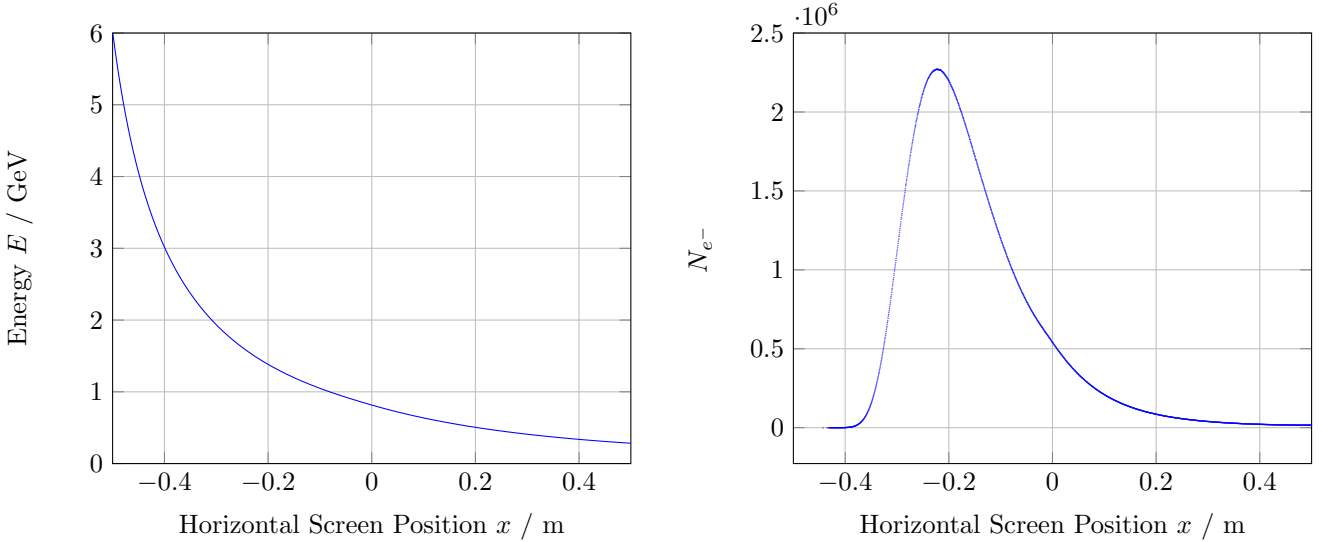
more accurate measurement of the beam parameters. The effect of the emittance and quadrupoles on the horizontal spread is taken to be negligible in comparison to the effect of the dipole, so it's effect is taken into account by adding a horizontal smearing to the horizontal position of each electron on the screen. This means that this plot in Figure 3a is all that is required to simulate the transverse spread of the beam.

The drift distances from the second quadrupole to the screen were also recorded for each  $x$  position on the screen. This function  $d(E(x))$  is used in the calculation of the vertical beam size.

### 5.1.2 Deriving the Beam Size Function

The dipole spreads the beam horizontally across the screen. The electrons in each vertical strip of pixels are grouped together and their energy approximated to be equal. This is allowed as the energy spread in each strip will always be less than 0.5%. This was calculated from data used to plot Figure 3a, by finding the ratio between the difference in energies between adjacent strips, by the energy value at that strip. This was done for all strips and the maximum value was a 0.5% difference in energy.

Using this assumption, we are able to create one beam and transport matrix for electrons in each vertical stream of pixels. The root mean square of the vertical beam size on the screen can be extracted



(a) Electron energies corresponding to the horizontal screen position due to the effect of the dipole.

(b) The number of electrons expected to hit the screen at each  $x$  position for  $E = 1.3$  GeV and  $\sigma_E = 0.4$  GeV.

Figure 3: The functions  $E(x)$  and  $N_{e-}(x)$  extracted from the BDSIM calibration output data. These functions are used to calculate the horizontal spread of the electrons across the screen.

from the resultant beam matrix  $\sigma_1$ . To arrive at this beam matrix, the transport matrix  $\mathcal{M}$  is applied to the initial beam matrix  $\sigma_0$  using (11). The transport matrix is the product of the transport matrices of each component of the spectrometer:

$$\mathcal{M} = \mathcal{M}_D(d) \cdot \mathcal{M}_{QD}(l_2) \cdot \mathcal{M}_D(g_2) \cdot \mathcal{M}_{QF}(l_1) \cdot \mathcal{M}_D(g_1) \quad (12)$$

where  $\mathcal{M}_D$  is the drift transport matrix which is a function of the travel distance and  $\mathcal{M}_{QF}$  and  $\mathcal{M}_{QD}$  are the transport matrices of the quadrupole.  $g_1$  is the drift distance (the gap) between the end of the plasma cell and the first quadrupole,  $g_2$  is the gap between the two quadrupoles,  $l_1$  and  $l_2$  are the effective quadrupole lengths of the focusing and defocusing quadrupoles respectively.  $d$  is the drift distance between the second quadrupole and the screen, taking into account the effect of the dipole, hence, is a function of the energy which was calculated in the BDSIM calibration stage.

For simplicity, it is assumed that the quadrupoles strengths  $k_1$  and  $k_2$  are set to values such that each quadrupole focuses at the mean energy of the beam, hence these variables are proportional to the beam's mean energy.

By applying the matrix multiplication the vertical beam size as a function of the horizontal screen

position can be extracted:

$$\begin{aligned} \sigma_y^2 = \sigma_{1,11} = & C^2(x)\sigma_{0,11} \\ & + 2C(x)S(x)\sigma_{0,12} \\ & + S^2(x)\sigma_{0,22} \end{aligned} \quad (13)$$

Using this beam spread function, a Gaussian distribution of electrons for each vertical pixel strip is generated with  $\sigma_y^2$  used as the variance of the distribution. After generating, a two dimensional histogram representing the number of electrons hitting the screen at each pixel the goal is to simulate the effectiveness of the equipment and the effect of background noise then translate this number to represent the raw signal that will be received from the camera.

## 5.2 Backgrounds

How good the measurement of the emittance is, is most dependant on the magnitude of the multiple sources of backgrounds as well as the reliability of the equipment. The following sources of error were taken into account: the efficiency of the scintillator screen, the acceptance of the camera due to it's distance from the scintillator screen, the background photon density, the emittance of photoelectrons in the camera, the thermal noise in the camera, the amplification by the microchannel plate (MCP) and the readout noise. Each source of noise is added to each pixel independently.

The first two error sources, the scintillator screen and the camera acceptance, both scale the original signal. So for each electron that hits the screen, it is expected that an average of 5000 photons are to be emitted radially with a cosine distribution. The camera acceptance, is the ratio of photons that the camera registers to the number of photons emitted by the scintillator, with a value of  $1.5 \times 10^{-5}$ . After the addition of these two effects, the camera is expected to receive 7.5 % of the original electron signal. The expected value for the number of photons incident on the camera due to the beam electrons is a Poisson random number.

It is assumed that there is a uniform distribution of photons incident on the camera. The density of these electrons is expected to be  $3.415 \times 10^4$  photons/m<sup>2</sup> equating to 0.01 background photons per pixel during the  $3 \times 10^{-3}$  s the gate is open. The number of background photons that hits a pixel is a discrete value, and so is also generated by generating a Poisson random number. As discussed later in Section 6 this value is very small in comparison to the signal produced by the beam and will only have an effect if the density of background photons is multiple magnitudes larger than the expected value.

The camera's photomultipliers then convert the photons of light back to an electrical current. This multiplies the incident number of photons by the quantum efficiency of the camera, 0.15. The expected number of thermal photoelectrons per pixel per second is expected to be 0.016 [25], with the camera running at the expected temperature of  $-30^\circ\text{C}$  with  $16^\circ\text{C}$  cooling water and an ambient room temperature of  $16^\circ\text{C}$ . This value is typically doubles for each  $5^\circ\text{C}$  rise in temperature of the camera [25]. At these running temperatures of the camera, about 9 photoelectrons are expected to be generated during the time the gate is open, which is an insignificant proportion in comparison to the beam signal, creating  $1 \times 10^7$  photoelectrons before MCP amplification.

The microchannel plate amplifies the number of photoelectrons by 1442, also amplifying all previously added backgrounds as well. This was simulated by scaling the value of the bin, and it's error, by 1442 rather than generating a Poisson random number. The modelling of this process may not be reflect the true nature of this process due to an uncertainty in underlying process, however the overall

effect remains accurately simulated. Despite this, the error arising from this process is likely to scale the error as mentioned.

And finally, before the values of the signal is obtained, a readout noise is added. This background is expected to add 7.2 readout electrons per image pixel for the camera operating at 1 MHz.

### 5.2.1 Error Calculations

Poisson statistics were used for the calculation of errors. Once the shape of the incident beam on the screen was calculated the number of electrons incident on each pixel was given an error of the square root of the count. Two methods of error propagation were used depending on the nature of the process involved. The following processes were modeled as additive processes: background photons hitting the screen, the thermal electrons from the currents in the camera and the readout noise, whereas the multiplicative processes are: photon generation at the scintillator screen, photoelectron generation in the camera PMTs and the amplification of the electron signal by the MCP.

Basic error propagation techniques were used here. For the additive processes, where the new value of each bin  $n$  is the sum between the old bin value  $n_0$  and the value given by the process  $n_{\text{proc}}$ :  $n = n_0 + n_{\text{proc}}$  the propagation of error is given by calculating the hypotenuse of the absolute errors:

$$\Delta n = \sqrt{\Delta n_0^2 + \Delta n_{\text{proc}}^2} \quad (14)$$

where the error of a Poisson random number is the square root of the value.

For the multiplicative processes, i.e.  $n = \lambda_{\text{proc}} n_0$  where  $\lambda_{\text{proc}}$  is the scaling factor of the process the propagation of the error is given by calculating the hypotenuse of the percentage errors:

$$\Delta n = n \sqrt{\left(\frac{\Delta n_0}{n_0}\right)^2 + \left(\frac{\Delta \lambda_{\text{proc}}}{\lambda_{\text{proc}}}\right)^2} \quad (15)$$

Many of the errors  $\Delta n_{\text{proc}}$  and  $\Delta \lambda_{\text{proc}}$  were unavailable at the time of simulation. All background noises are modeled as uniformly distributed Poisson random numbers so under these assumptions the associated error on each value can correctly be taken

to be the square root of the value. So for missing  $\Delta n_{\text{proc}}$  values, (14) becomes

$$\Delta n = \sqrt{\Delta n_0^2 + n} \quad (16)$$

and for multiplicative processes, the resultant values were also Poisson random numbers meaning (15) can be rewritten as

$$\Delta n = n \sqrt{\left(\frac{\Delta n_0}{n_0}\right)^2 + \left(\frac{\sqrt{n}}{n}\right)^2} \quad (17)$$

where the full statistical error of the generated value is taken into account without knowledge of the error of the scaling factor.

### 5.3 Calculating the Emittance

The signal received from the camera is required to be scaled back to represent the real beam size on the screen. The effect of additive backgrounds and scaling processes are reverted in the reverse order of their application arriving at a measured value for the number of electrons that hit the screen at each pixel.

To calculate the vertical beam size for each pixel strip, a Gaussian function is fitted to the vertical beam profile using CERN ROOT's  $\chi^2$  minimising fitting algorithm [26]. The root mean square of the fitted Gaussian is then calculated for each strip to obtain the vertical beam size at each horizontal position on the screen. These points are displayed as the black points in the beam reconstruction plots in Figures 4 and 5.

Finally, the vertical beam size function, previously used to simulate the shape of the incident electron beam, is then fitted to the measured beam sizes. Again, the fitting is done wholly using ROOT's  $\chi^2$  minimising fitting algorithm, where the three beam parameters  $\epsilon$ ,  $\beta$  and  $\gamma$  as parameters to be minimised.

## 6 Results

Along with the  $\chi^2$  minimised parameter values of the fit, each simulation generated a plot, showing the simulated, measured and fitted vertical beam size functions as a function of horizontal position  $x$  on the screen. Figure 4 is the output of a run with

all parameters set to their expected values. Figure 5 is an output plot for a run with a small (1 %) energy spread so the spread of the beam is very narrow across the screen, so this plot is essentially zoomed in at a small section of the screen. The solid black line is the shape of the simulated electron beam that hits the screen, the black points show the simulated measurements of the RMS width of the fitted Gaussian for each vertical strip of pixels. The blue dashed line is the beam size function fitted to the points.

### 6.1 Binning errors

After the investigation of multiple experimental parameters, the emittance measurement consistently converged to a value  $1 \times 10^{-8}$  larger than the input emittance. The reason for this systematic error was found to be due to the discretization of the beam hitting the screen meaning that the measurement of the vertical beam size was consistently overestimated. Since the electrons in each pixel are not uniformly distributed but rather more densely distributed closer towards the mean value, giving rise to a systematic overestimation of the vertical beam size of up to two times the vertical size of the pixel. This effect can be seen most clearly when a very small energy spread was used as can be seen in Figure 5, where the measured beam heights are consistently larger than the actual beam height.

This systematic error is displayed in subsequent plots as a blue line, where the red line shows the true beam emittance and the blue line represents where the emittance measurement should be taking into account this error.

### 6.2 Energy Spread

Initially, the mean energy of the beam and energy spread of the beam were tested independently. Simulations for all combinations of the following energies  $E \in \{0.5, 1, 1.3, 2.0, 3.05, 0\}$  and the following energy spreads  $\sigma_E \in \{0.01, 0.1, 0.3, 0.4\}$  were run. These energies and energy spreads were chosen such that at least one full standard deviation of the beam hit the screen. As Figure 3a shows, the range of energies that hit the screen for this setting of the dipole and quadrupole, is from  $\sim 0.28$  GeV to 6 GeV.

The smaller the energy spread of the beam the smaller the spread of the beam across the screen.

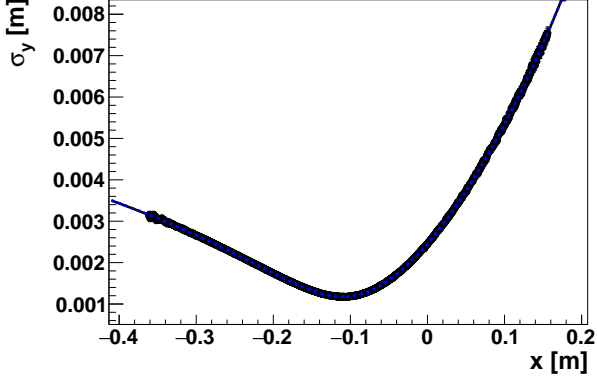


Figure 4: The beam reconstruction (blue line) of a simulation run with all the expected parameter values.  $E = 1.3$  GeV,  $\sigma_E = 0.4$  GeV,  $\epsilon = 1$  mm mrad

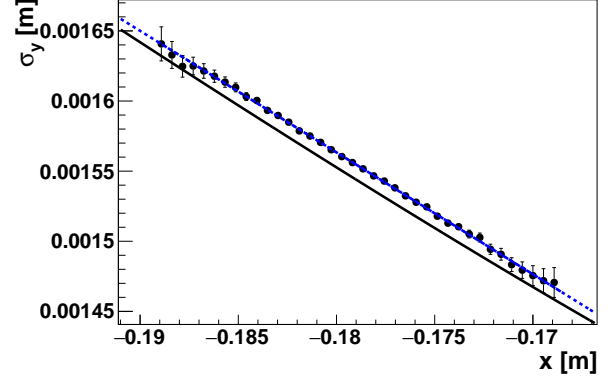


Figure 5: The beam reconstruction, consistently overestimates the vertical beam size. This run used a small percentage energy spread of 1%. With all other parameters set to their expected value.

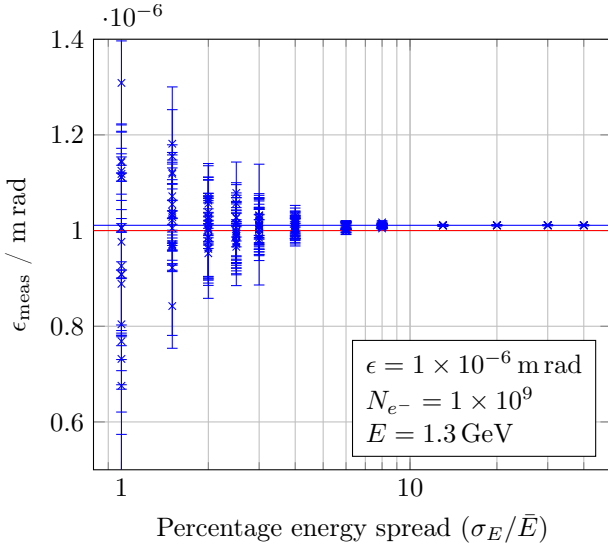


Figure 6: Plot of the simulated emittance measurement against the percentage spread of the beam energy, showing emittance measurements becoming unreliable at percentage energy spreads below 2%.

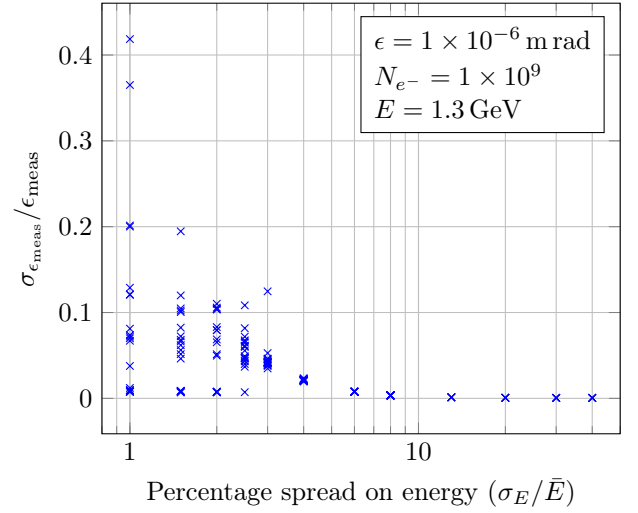


Figure 7: Plot of the simulated emittance measurement errors against the percentage spread of the beam energy, showing an exponential increase in the spread of the errors as the percentage error spread is narrowed.

Figure 5 is a plot showing the full spread of the beam across the screen for a beam energy spread of 1%. The fewer vertical beam measurements that the function is able to fit to, the larger the errors of the measured emittance and the energy spread in Figure 6 is the expected result. The expected energy spread, 0.4 GeV, translates to a percentage energy spread of 30% at the expected beam energy of 1.3 GeV. By this point, the error on the measurement of the emittance has converged to less than a 1%.

Plotting the absolute simulated measurement er-

ror against the percentage energy spread in Figure 6 it is clearer the manner in which the errors blow up for lower energy spreads. For lower energy spreads, all measurement errors were expected to increase exponentially. However this is not the case, but rather, the *spread* of measurement errors increased exponentially, meaning that may measurement errors are still only a few percent of the measurement. This behaviour reflects how the errors for the background noise were calculated; the error associated with the background photons for each pixel is set to the square root of the number of background photons. This means the fewer the number of incident

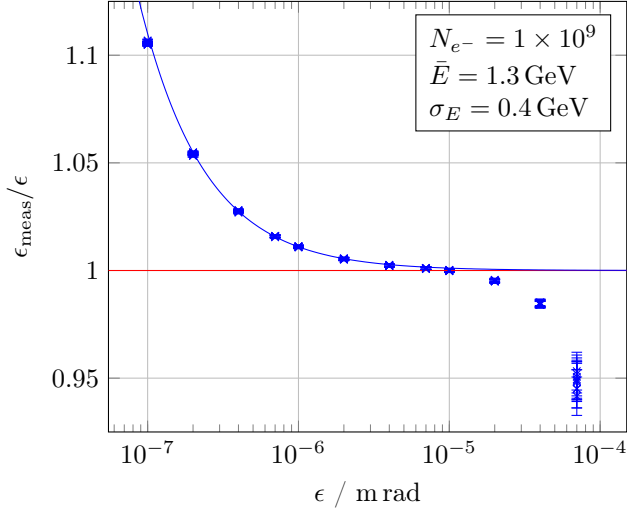


Figure 8: Plot of the ratio between the measured and true emittances of the beam against the true emittance of the beam. The blue line is the expected measurement value when taking into account the systematic overestimation due to discrete bins.

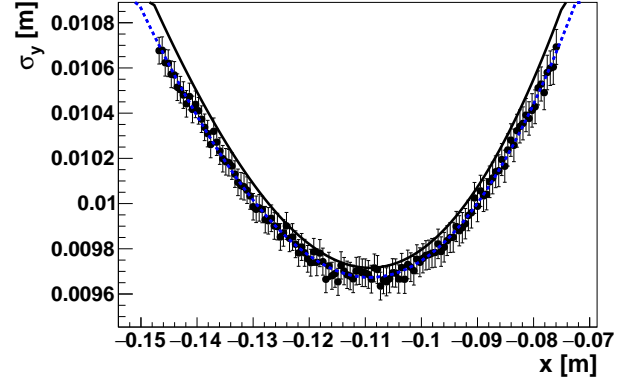


Figure 9: Beam reconstruction for a large beam emittance of  $7 \times 10^{-5}$  mrad showing the underestimation of the measured vertical beam sizes.

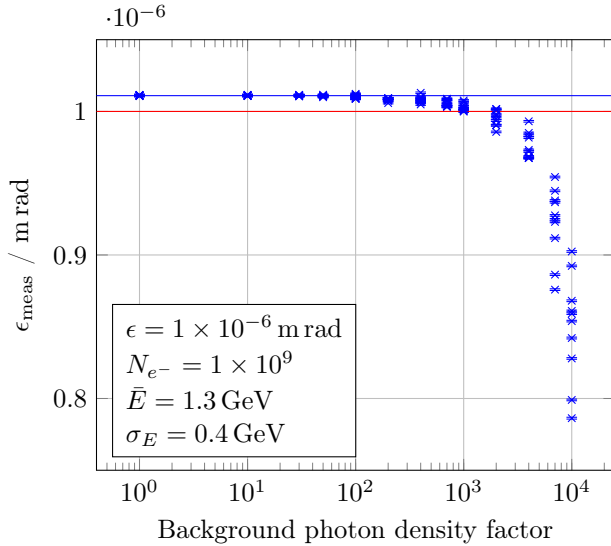


Figure 10: Plot of the measured beam emittance against a factor of the expected background density of  $3.415 \times 10^4$  photons/m<sup>2</sup>

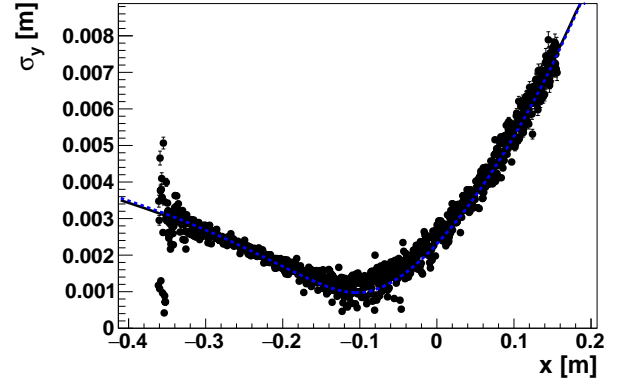


Figure 11: Beam reconstruction for a background  $1 \times 10^4$  times the expected background photon density.

background photons the screen, the smaller the error. However, the error in the uncertainty of the measurement of the background was not taken into account then scaling the raw signal back into the real shape. This extra error arises from the uncertainty in the measurement of the background photon density when there is no accelerated electron beam. To take this into account, this error must be added in quadrature to each pixel.

The upper ranges of this energy spread may also be investigated, however, this is less of a priority.

Percentage energy spreads up to 80 % were investigated without signs of alterations to the measured emittance of emittance measurement. It is expected that as the beam energy moves outside the 0.28 GeV to 6 GeV range, emittance measurements will become more erroneous since most of the beam will not hit the screen.



### 6.3 Input Emittance

Since the emittance is the parameter required to be measured, a reasonably large region around the expected emittance should give precise emittance measurements. The input beam emittance range tested was from  $1 \times 10^{-7}$  mrad to  $1 \times 10^{-4}$  mrad as shown in Figure 8. Emittances below  $10^{-5}$  mrad showed accurate emittance measurements, with the  $\sim 10^{-8}$  mrad overestimation of the emittance measuring persisting over this range.

Increasing the emittance of the beam above  $10^{-5}$  mrad results in an underestimation in the measurement of the emittance as well as an increase in the measurement's error. This behaviour is expected. Increasing the emittance of the beam means the spread of the beam on the screen is larger. At emittances above  $10^{-5}$  mrad, a significant proportion of the beam's electrons no longer hit the 6.5 cm tall screen, so particles with the largest transverse momentum no longer contribute to the emittance measurement. Figure 9 displays this effect showing that the shape of the beam on the screen is a lot less focused in the vertical axis and each vertical beam size measurement is underestimated in comparison to the run of expected parameters in Figure 4.

### 6.4 Background Photons

This background noise is the most likely source of error to change during and between runs, as all other sources of error arise from intrinsic properties of the equipment, or from the setup of the experiment. The background photon noise is expected to be almost insignificant in comparison to the signal of the beam, where the ratio of signal to background photons is expected to be in the order of magnitude  $4 \times 10^4$ . The aim was to find the level of background photon radiation at which the measurement of the emittance would be strongly affected. The expected background density was multiplied by an arbitrary factor until the emittance value deviated from the true value. Figure 10 shows how this factor affects the measurement. Only after the expected background has been multiplied by a factor of  $\sim 100$  is any effect seen on the measured emittance. Between background factors  $10^2$  and  $10^3$  the measured emittance begins to be underestimated and above a background factor of  $10^3$  the emittance measurement becomes increasingly imprecise with a deviation a few

percent at a background factor of  $2 \times 10^3$ , increasing up to 10 % at a background factor of  $10^7$ .

The reasoning for a larger spread in the measured emittance values comes from the background drowning out the signal, that is, the fluctuations of the randomly generated background between the pixels become large enough to distort the shape of the image on the screen. The amount by which the image is distorted is not taken into account by the error bars in Figure 10, suggesting that error in the background was not completely accounted for. The absence of this error is propagated to the error of the emittance measurement, as can be seen in Figure 10, as the error significantly underestimates the fluctuations in the measurement. However, these error bars can be inferred from the spread of the measurements since for lower backgrounds all ten runs are closely grouped and for higher backgrounds there is a clear spread of measurement values.

## 7 Conclusion

In these simulations, certain properties of the accelerated electron beam were approximated in order to simplify the simulation. These approximations assume that the beam has a Gaussian energy spread and that its phase space distribution was well defined by the enclosing ellipse. Whereas the energy spread of the beam will more likely be skewed and its distribution in phase space will have 'tails' extending from the central ellipse. The difference these approximations make to the accuracy of the simulations carried out in this report, is assumed to be quite small. A change in the energy distribution will only alter the density of electrons on the screen and the number electrons in the 'tails' of the phase space are expected to be three orders of magnitude less dense than the central phase volume.

The effect of three different experimental parameters were investigated, and the ranges between which the emittance measurements were accurate and reasonably precise were found. Despite the fact that the error measurements were miscalculated, these can be inferred from the spread of these measurements. So the behaviour of the emittance measurement with respect to these parameters have been presented.

There still remains many possible combinations of these parameters to be investigated. For example at higher backgrounds, the range of percentage energy



spreads where an emittance measurement would be reliable is likely to shift. For this reason, the expected values for all other parameters that were not being investigated were used.

## References

- [1] Martin Flechl. “Higgs boson discovery and recent results”. In: *22th International Workshop on High Energy Physics and Quantum Field Theory (QFTHEP 2015) Samara, Russia, June 24-July 1, 2015*. 2015. arXiv: [1510.01924 \[hep-ex\]](#). URL: <http://inspirehep.net/record/1396561/files/arXiv:1510.01924.pdf>.
- [2] CMS Collaboration. “First measurement of the differential cross section for ttbar production in the dilepton final state at  $\sqrt{s} = 13$  TeV”. In: (2015).
- [3] R. Barate et al. “Search for the standard model Higgs boson at LEP”. In: *Phys. Lett. B* 565 (2003), pp. 61–75. DOI: [10.1016/S0370-2693\(03\)00614-2](#). arXiv: [hep-ex/0306033 \[hep-ex\]](#).
- [4] K. Oide. “Synchrotron Radiation Limit on the Focusing of Electron Beams”. In: *Phys. Rev. Lett.* 61 (1988), pp. 1713–1715. DOI: [10.1103/PhysRevLett.61.1713](#).
- [5] A. A. Sokolov and I. M. Ternov. “Synchrotron radiation”. In: *Akademia Nauk SSSR, Moskovskoie Obshchestvo Ispytatelei prirody. Seksia Fiziki. Sinkhrotron Radiation, Nauka Eds., Moscow, 1966 (Russian title: Sinkhrotronnoie izluchenie), 228 pp.* (1966).
- [6] Lucie Linssen et al. “Physics and Detectors at CLIC: CLIC Conceptual Design Report”. In: (2012). DOI: [10.5170/CERN-2012-003](#). arXiv: [1202.5940 \[physics.ins-det\]](#).
- [7] Ties Behnke et al. “The International Linear Collider Technical Design Report - Volume 1: Executive Summary”. In: (2013). arXiv: [1306.6327 \[physics.acc-ph\]](#).
- [8] T. Tajima and J. M. Dawson. “Laser electron accelerator”. In: *Phys. Rev. Lett.* 43 (1979), pp. 267–270. DOI: [10.1103/PhysRevLett.43.267](#).
- [9] W. Lu et al. “Generating multi-GeV electron bunches using single stage laser wakefield acceleration in a 3D nonlinear regime”. In: *Phys. Rev. ST Accel. Beams* 10 (2007), p. 061301. DOI: [10.1103/PhysRevSTAB.10.061301](#). arXiv: [physics/0612227 \[physics\]](#).
- [10] Wim P. Leemans et al. “GeV electron beams from a cm-scale accelerator”. In: *Nature Phys.* 2 (2006), pp. 696–699. DOI: [10.1038/nphys418](#).
- [11] Allen Caldwell et al. “Proton Driven Plasma Wakefield Acceleration”. In: *Nature Phys.* 5 (2009), pp. 363–367. DOI: [10.1038/NPHYS1248](#), [10.1038/nphys1248](#). arXiv: [0807.4599 \[physics.acc-ph\]](#).
- [12] Naveen Kumar, Alexander Pukhov, and Konstantin Lotov. “Self-modulation instability of a long proton bunch in plasmas”. In: *Physical review letters* 104.25 (2010), p. 255003.
- [13] KV Lotov et al. “Natural noise and external wakefield seeding in a proton-driven plasma accelerator”. In: *Physical Review Special Topics-Accelerators and Beams* 16.4 (2013), p. 041301.
- [14] Carl Siemon et al. “Laser-seeded modulation instability in a proton driver plasma wakefield accelerator”. In: *Physics of Plasmas (1994-present)* 20.10 (2013), p. 103111.
- [15] J Vieira, WB Mori, and P Muggli. “Hosing instability suppression in self-modulated plasma wakefields”. In: *Physical Review Letters* 112.20 (2014), p. 205001.
- [16] Helmut Wiedemann. *Particle accelerator physics I*. Berlin, Germany: Springer, 1999. ISBN: 9783540490432, 9783662038277. DOI: [10.1007/978-3-662-03827-7](#). URL: <http://www.springer.com/us/book/9783662038277>.
- [17] E. Öz, F. Batsch, and P. Muggli. “An accurate Rb density measurement method for a plasma wakefield accelerator experiment using a novel Rb reservoir”. In: *Nucl. Instrum. Meth. A* 829 (2016), pp. 321–325. DOI: [10.1016/j.nima.2016.02.005](#). arXiv: [1511.08763 \[physics.ins-det\]](#).
- [18] Erdem Öz, Fabian Batsch, and Patric Muggli. “A Novel Laser Ionized Rb Plasma Source for Plasma Wakefield Accelerators”. In: *Proceedings, 5th International Particle Accelerator Conference (IPAC 2014): Dresden, Germany, June 15-20, 2014*. 2014, TUPME073. URL: <http://jacow.org/IPAC2014/papers/tupme073.pdf>.
- [19] J. Vieira et al. “The ion motion in self-modulated plasma wakefield accelerators”. In: *Phys. Rev. Lett.* 109 (2012), p. 145005. DOI: [10.1103/PhysRevLett.109.145005](#). arXiv: [1208.3242 \[physics.plasm-ph\]](#).
- [20] J. Vieira et al. “Ion motion in the wake driven by long particle bunches in plasmas”. In: *Phys. Plasmas* 21 (2014), p. 056705. DOI:

[10.1063/1.4876620](#). arXiv: [1409.4328](#)  
[physics.plasm-ph].

- [21] Lawrence Deacon et al. “A Spectrometer for Proton Driven Plasma Accelerated Electrons at AWAKE - Recent Developments”. In: *Proceedings, 7th International Particle Accelerator Conference (IPAC 2016): Busan, Korea, May 8-13, 2016*. 2016, WEPMY024. DOI: [10.18429/JACoW-IPAC2016-WEPMY024](#). URL: <https://inspirehep.net/record/1470272/files/wepmy024.pdf>.
- [22] Jean Buon. “Beam phase space and emittance”. In: *CERN European Organization for Nuclear Research-Reports-CERN* (1994), pp. 89–89.
- [23] I Agapov et al. “BDSIM: A particle tracking code for accelerator beam-line simulations including particle-matter interactions”. In: *Nuclear Instruments and Methods in Physics Research Section A: Accelerators, Spectrometers, Detectors and Associated Equipment* 606.3 (2009), pp. 708–712.
- [24] Sea Agostinelli et al. “GEANT4 - A simulation toolkit”. In: *Nuclear instruments and methods in physics research section A: Accelerators, Spectrometers, Detectors and Associated Equipment* 506.3 (2003), pp. 250–303.
- [25] *Hardware Guide for the iStar Intensified sCMOS camera*. Version 1 rev 19. ANDOR an Oxford Instruments company. Andor Technology Ltd., 7 Millennium Way, Springvale Business Park, Belfast, BT12 7AL, Northern Ireland, Sept. 2016.
- [26] R. Brun and F. Rademakers. “ROOT: An object oriented data analysis framework”. In: *Nucl. Instrum. Meth.* A389 (1997), pp. 81–86. DOI: [10.1016/S0168-9002\(97\)00048-X](#).